Check for updates

First-principles-based microkinetic modeling of methanol steam reforming over Cu(111) and Cu(211): structure sensitive activity and selectivity†

Xinyi Zhang and Bo Yang [ID] *

The development of hydrogen energy is widely recognized as a key approach to addressing the energy and carbon emission challenges. Methanol steam reforming is a promising hydrogen production scheme that can provide high-purity hydrogen. In this work, we studied the primary reaction mechanisms of methanol steam reforming over the Cu(111) and Cu(211) surfaces using density functional theory (DFT) calculations and microkinetic simulations. A detailed kinetic perspective on the reaction mechanism, which is often overlooked in previous research that relies solely on DFT calculations, is provided in the current work. Our findings reveal that under typical experimental conditions, the dominant mechanism on the Cu(111) surface is the methyl formate mechanism, while the H_2COO dehydrogenation mechanism is dominant on Cu(211). The activity over the Cu(111) surface was slightly higher than that over Cu(211). Based on the degree of rate control analysis results, a reaction rate equation was derived to quantitatively explain the trend of activity under different operating conditions. It was also found that CO_2 selectivity was significantly higher over Cu(211) than over the Cu(111) surface. Furthermore, based on the Wulff construction scheme, copper nanoparticle models with different sizes were constructed, and a detailed structure sensitivity study was executed. This comprehensive investigation sheds light on the mechanisms of methanol steam reforming reactions over the Cu(111) and Cu(211) surfaces, providing essential insights for the design of high-performance catalysts for hydrogen production.
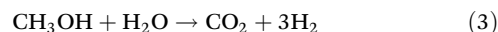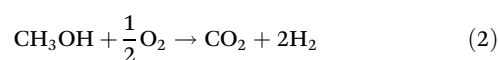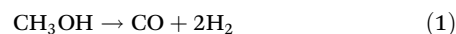
1. Introduction

As the urgency of the energy crisis intensifies and environmental pollution worsens, the search for novel energy sources is more pressing than ever.[1–3] Hydrogen, a high-energy-density, clean and renewable secondary energy source, is widely regarded as a crucial alternative to fossil fuels.[4–6] It can be produced through various methods, including methane steam reforming, coal gasification, electrolysis of water, and biological methods.[7] However, the first two methods still rely on fossil fuel as raw material, and the third method requires substantial energy input.[8] Therefore, exploring a new approach to produce hydrogen with high efficiency and minimal pollution is of the utmost importance.

Methanol serves as an ideal substrate for producing hydrogen due to its simple molecular structure and easy accessibility.[9] It can be derived from various renewable sources. For instance, it can be produced through the pyrolysis of biomass,

which includes components such as cellulose, hemicelluloses, and lignin,[10] or through the thermal gasification of biomass.[11] There are three primary methods to produce hydrogen with methanol, *i.e.*, (1) methanol decomposition, (2) oxidative methanol steam reforming, and (3) methanol steam reforming:

$$CH_3OH \rightarrow CO + 2H_2 \tag{1}$$

$$CH_3OH + \frac{1}{2}O_2 \rightarrow CO_2 + 2H_2 \tag{2}$$

$$CH_3OH + H_2O \rightarrow CO_2 + 3H_2 \tag{3}$$

Among the three methods mentioned above, methanol steam reforming (MSR) holds promise for producing hydrogen due to its high yield of H_2 and significant selectivity towards CO_2.[12] This selectivity towards CO_2 is crucial for further hydrogen utilization,[13] because even minuscule amounts of carbon monoxide (CO) can be harmful under many circumstances, necessitating an exceptionally pure and CO-free hydrogen source.

In order to design new catalysts that enhance the activity of MSR and increase selectivity towards CO_2, it is essential to understand the detailed reaction mechanism. Cu-based cata-

School of Physical Science and Technology, ShanghaiTech University, 393 Middle Huaxia Road, Shanghai 201210, China. E-mail: yangbo1@shanghaitech.edu.cn

lysts are predominantly used for MSR due to their high activity and selectivity.[14] The current mainstream view proposes three mechanisms for MSR over Cu, with the first step in each mechanism being the dehydrogenation of methanol to form methoxy.[12,14] One of the three mechanisms is the water gas shift (WGS) mechanism.[15–17] This mechanism involves the decomposition of methanol to CO, which further reacts with water vapor to yield CO_2. However, studies have shown that CO cannot react with water vapor in the presence of methanol, despite the WGS reaction being highly active on Cu-based catalysts.[18]

An alternative mechanism was proposed by Takezawa, which involves formaldehyde reacting with hydroxyl or oxygen adsorbed on the catalyst surface to produce intermediates such as HCOOH, HCOO, and H_2COO.[19] These species are further dehydrogenated and eventually converted to CO_2 and H_2. This mechanism is referred to as the H_2COO dehydrogenation mechanism.

Takezawa also proposed the methyl formate mechanism suggesting that formaldehyde reacts with methoxy to form methyl formate, which is then hydrolyzed and dehydrogenated to form CO_2.[20] Jiang[21] and Peppley[22] established a kinetic model based on this mechanism, and their results were highly consistent with experimental data, indicating that the methyl formate mechanism is likely responsible for MSR. However, methyl formate is generally produced at a lower proportion of water vapor and cannot be detected in the gas phase or on the surface of the catalyst under MSR conditions.[23] Although it has been demonstrated that the rate of methyl formate hydrolysis to CO_2 is approximately 30 times faster than that of the overall MSR reaction, which implies that the absence of methyl formate may be due to its hydrolysis occurring too rapidly to be observed, the fact that methyl formate is not directly observed in experiments still raises questions about the authenticity of this proposed mechanism.[20]

Despite extensive research on the mechanism of MSR over Cu, this topic remains contentious. Given the inherent challenges in experimentally elucidating the actual reaction mechanism of MSR, computational simulation methods, such as first-principles calculations, have become vital in providing complementary and often more detailed information about the reaction mechanism.

Regarding the methyl formate mechanism, the work of Lin et al.[24] calculated the energy of each intermediate and transition state involved in this mechanism on the Cu(111) surface and found that the methyl formate mechanism is energetically favored. This process was shown to have a lower effective activation energy than the overall MSR reaction, which is consistent with the experimental observation that the steam reforming of methyl formate is faster than the MSR reaction. Lin et al. also found that the hydrolysis process of methyl formate may not be able to effectively compete with the desorption of methyl formate. Therefore, they concluded that the methyl formate route is not a competitive mechanism on the Cu(111) surface. While their study focused primarily on the energetics over the Cu(111) surface, the exact reaction mechanism over

different facets of the copper catalyst and the identification of the most active facet still remain unknown. Thus, it would be valuable to compare their results with a comprehensive microkinetic study over both the Cu(111) and Cu(211) facets.

In the present study, a comprehensive analysis was conducted. We employed density functional theory (DFT) calculations to determine the energies of surface species on the Cu(111) and Cu(211) facets, based on the establishment of a complex reaction network. Furthermore, detailed microkinetic analysis was also performed to gain deeper insights into the reaction system. The dominant reaction pathway under each set of reaction conditions was determined from the reaction network under different operating conditions. The activity of the MSR reaction, CO_2 selectivity, and the detailed reaction mechanisms were also systematically studied and compared on both the Cu(111) and Cu(211) surfaces.

2. Methods

2.1 DFT calculations

All the DFT calculations performed in this study were carried out using the Vienna Ab initio Simulation Package (VASP.5.4) and the projector augmented wave (PAW) method.[25–27] The Bayesian error estimation functional with van der Waals correlation (BEEF-vdW) exchange–correlation functional was employed,[28] which can account for long-range dispersion forces and has been widely used in the simulation of surface catalytic reactions.[29–37] The plane-wave basis set had a cutoff energy of 500 eV, and the convergence criteria were set to 1×10^{-4} eV for energy and 0.05 eV Å^{-1} for the force on each relaxed atom. The 3×3 Cu(111) slab model consisted of 5 atomic layers, with the atoms in the top 2 layers allowed to relax during the optimization process. For the 3×4 Cu(211) slab model, there were 12 atomic layers, and the atoms in the top 3 layers were allowed to relax during the optimization. The Brillouin zone was sampled using a $4 \times 4 \times 1$ Monkhorst–Pack k-point grid with Methfessel-Paxton smearing of 0.1 eV for the Cu(111) surface,[38] and a $4 \times 2 \times 1$ k-point grid for the Cu(211) surface.

The transition states were determined using the constrained minimization method.[39,40] This approach allows for the identification of a transition state when the force on the relaxed atom diminishes and the energy is maximized along the reaction coordinate but minimized with respect to all remaining degrees of freedom. The constrained minimization method has been developed for more than twenty years and is widely used by many groups and verified by frequency calculations.[41–44] All transition states were verified by vibrational frequency analysis, and the obtained vibrational frequencies were also used to calculate the associated free energies. The adsorption enthalpy of CO over Cu(111) calculated by DFT data is −0.656 eV. According to the adsorption energy measured experimentally (−0.549 eV),[45] the gas-phase energy of molecular CO was corrected by −0.107 eV. The reaction free energy of methanol steam reforming calculated by CatMAP under 298 K temperature and standard pressure is

−0.3177 eV. The energy of gaseous CO_2 was corrected by 0.278 eV to align with the experimental value[46] (−0.0397 eV) of the Gibbs free energy of reaction for the methanol steam reforming reaction.

2.2 Microkinetic modeling

The reaction kinetics of the MSR process were analyzed using the CatMAP package developed by Nørskov's group.[47] This Python-based simulation package applies the mean-field approximation to obtain the kinetic results of surface catalytic reactions. According to the experimental conditions, simulations were performed at 5% CH_3OH conversion, with a temperature range of 498–598 K and a total pressure of 1 bar. The steam-to-methanol partial pressure ratios (S : M) were set to 1 : 1, 1 : 2, 1 : 3, and 1 : 4 to investigate the variation of the reaction mechanism under different S : M ratios. In this study, the variation in the S : M ratio was achieved by altering the partial pressure of water vapor, while keeping the partial pressure of methanol constant at 0.15 bar, the remaining composition was inert gas. The partial pressure of the inert gas was adjusted to compensate for the varying partial pressure of water vapor, ensuring that the sum of the partial pressures of all gaseous species remains constant. The free energies of the surface species and transition states were calculated using the following equation:

$$G(T) = E_{\text{DFT}} + E_{\text{ZPE}} + \sum_i^{\text{harmonic DOF}} \left[\frac{h\nu_i}{e^{\frac{h\nu_i}{k_B T}} - 1} \right] - T \cdot S(T) \quad (4)$$

where E_{DFT} is the DFT energy, E_{ZPE} is the zero-point energy, ν_i is the vibrational frequency along the harmonic degree of freedom (DOF), k_B is the Boltzmann constant, and h is the Planck constant. $S(T)$ is the entropy of the surface species, which can be determined using the equation:

$$S(T) = k_B \sum_i^{\text{harmonic DOF}} \left[\frac{h\nu_i}{k_B T \left(e^{\frac{h\nu_i}{k_B T}} - 1 \right)} - \ln\left(1 - e^{-\frac{h\nu_i}{k_B T}} \right) \right] \quad (5)$$

The free energies of the gaseous species were determined by the equation:

$$G(T) = E_{\text{DFT}} + E_{\text{ZPE}} + \int_0^T C_p dT - T \cdot S(T) \quad (6)$$

where the heat capacity C_p and entropy $S(T)$ can be obtained using the Shomate equation and the corresponding parameters.[48]

The degree of rate control (DRC) analysis method developed by the Campbell group[49,50] was also employed in this study. The DRC value quantifies the effect of changing the free energy of a surface intermediate or transition state on the overall reaction rate. Specifically, the DRC value X_i for the considered intermediate or transition state i can be obtained using the following equation:

$$X_i = \frac{\partial \ln(r)}{\partial (-G_i/(k_B T))_{G_{j \neq i}}} \quad (7)$$

where r is the rate of the full reaction, G_i represents the free energy of species i, and T is the reaction temperature. For transition states, the DRC value is typically positive because lowering the energy of the transition state or the corresponding activation free energy increases the turnover frequency (TOF). The transition state with the highest DRC value is known as the rate-controlling transition state (RCTS). For surface-adsorbed intermediates, the DRC value is usually negative and is equal to the opposite of the product between the fraction of reaction sites required to complete the reaction and the coverage of that intermediate. The intermediate with the largest DRC in absolute value is referred to as a rate-controlling intermediate (RCI).

3. Results and discussion

3.1 Reaction network of the MSR process

In the present study, a complex reaction network was established, consisting of 24 surface intermediates, 51 transition states, 5 gaseous species, and 54 elementary steps. A full reaction network containing all surface species can be found in the ESI.† We found that the reaction network includes most of the intermediates considered in previously published theoretical works,[24,51–55] including intermediates and transition states for the methyl formate pathway, the H_2COO dehydrogenation pathway, and the water–gas shift pathway. The energies of all possible reaction intermediates and transition states involved in the networks were calculated for further analysis, and the activation free energies and reaction free energies for each elementary step are listed in the ESI as Table S1.†

3.2 Dominant reaction pathways for MSR

Microkinetic simulations were conducted using the established reaction network on the Cu(111) and Cu(211) surfaces at the temperatures and pressures employed in experiments, specifically 498 to 598 K and 1 bar. The dominant reaction pathways were identified under these conditions through running the microkinetic simulations and removing the elementary steps with the lowest reaction rates iteratively, as introduced in our previous work.[56] In this previous work, a systematic description of the algorithm for reaction network generation and pruning was provided, using the concept also proposed by our group.[57] The dominant reaction pathways for MSR are merged into a pruned reaction network shown in Fig. 1(a), where the elementary steps and surface species unique to pathways A and B are shown in blue and red, respectively. Fig. 1(b) presents the dominant reaction pathway under different conditions over the Cu(211) and Cu(111) surfaces. The reaction energies and activation energy for the elementary steps involved in the dominant pathways are provided in Table 1. The configurations for the intermediates and transition states in the elementary steps are presented in the ESI as Fig. S1.†
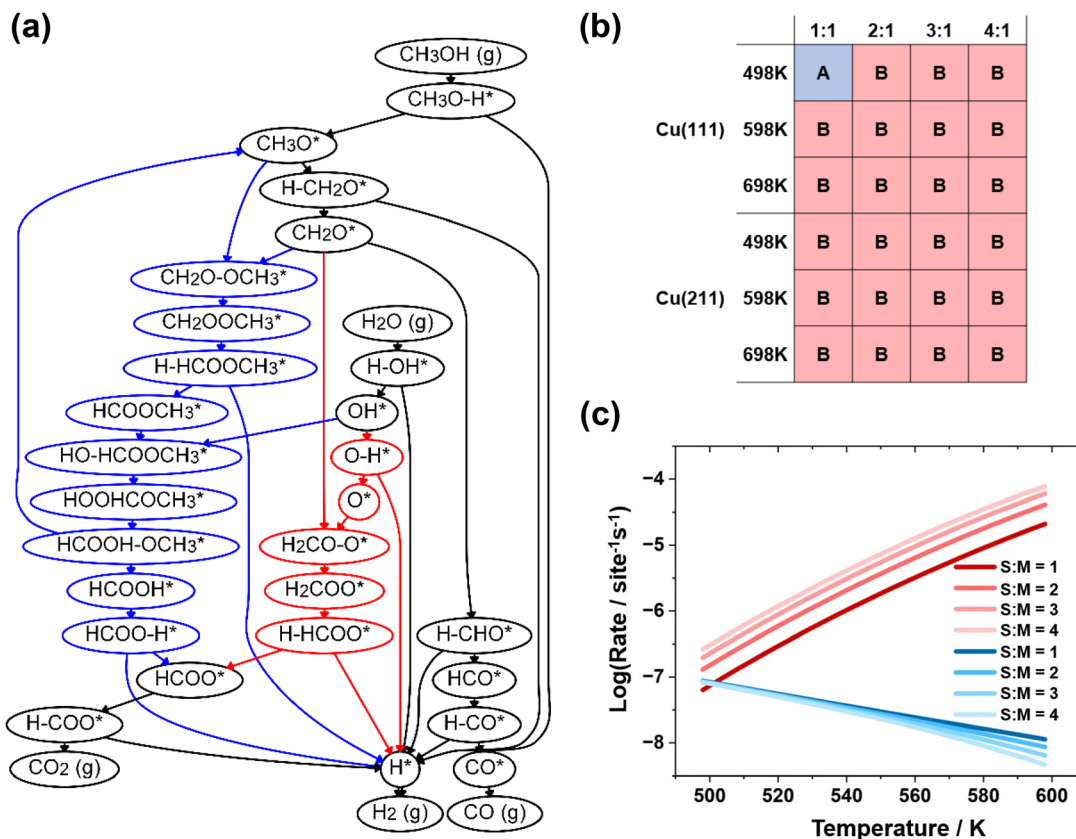
Fig. 1 (a) Pruned reaction network of the methanol steam reforming to CO and CO$_2$ on Cu(211) and Cu(111) after reaction network pruning, surface species and elementary steps only exist in pathway A are denoted by blue color, while those only exist in pathway B are denoted by red color. (b) Dominant reaction pathways over Cu(111) and Cu(211) under 2 different temperature and 4 different S : M ratios; different dominant reaction pathways are represented by A and B. (c) The variation of reaction rates of (1) CH$_2$O* + O* → H$_2$COO* + * and (2). CH$_2$O* + CH$_3$O* → CH$_2$OOCH$_3$* + *. Over different temperatures and S : M, while the reaction (1) contained in mechanism A is denoted by color blue and reaction (2) characteristic of mechanism B is denoted by color red.

Table 1 Activation energies (E_a) and reaction energies (ΔE), both in eV, for the elementary steps in the dominant reaction pathways of methanol steam reforming to CO and CO$_2$ on Cu(211) and Cu(111)

	Cu(111)		Cu(211)	
Elementary steps	E_a/eV	ΔE/eV	E_a/eV	ΔE/eV
2* + CH$_3$OH(g) → CH$_3$O* + H*	1.03	−0.31	1.03	−0.36
H$_2$O(g) + 2* → OH* + H*	1.20	−0.17	1.14	−0.35
OH* + * → O* + H*	1.82	0.63	1.76	0.94
CH$_3$O* + * → H* + CH$_2$O*	1.42	0.99	1.28	1.10
CH$_2$O* + O* → H$_2$COO* + *	−0.15	−0.66	0.04	−0.99
H$_2$COO* + * → HCOO* + H*	0.89	−0.79	0.96	−0.73
HCOOH* + * → HCOO* + H*	0.71	−0.39	0.69	−0.66
HCOO* + * → CO$_2$(g) + H* + *	1.19	0.70	1.52	1.14
CH$_2$O* + * → HCO* + H*	0.96	0.38	1.00	0.28
HCO* + * → CO* + H*	0.31	−0.75	0.38	−0.42
CH$_2$O* + CH$_3$O* → CH$_2$OOCH$_3$* + *	0.24	−0.43	0.10	−0.57
CH$_2$OOCH$_3$* + * → HCOOCH$_3$* + H*	1.01	0.02	1.17	0.32
HCOOCH$_3$* + OH* → HOOHCOCH$_3$* + *	0.56	0.27	0.70	0.23
HOOHCOCH$_3$* + * → HCOOH* + CH$_3$O*	0.37	−0.29	0.38	−0.10
H* + H* → H$_2$(g) + 2*	0.96	0.27	0.95	0.15
CO* → CO(g) + *	—	0.55	—	0.50

Analysis of the pruned reaction network shown in Fig. 1(a) reveals that pathway A is consistent with the methyl formate mechanism proposed by Takezawa,[20] while pathway B resembles the H_2COO dehydrogenation mechanism. Our results indicate that the methyl formate mechanism only exists at low temperatures and low S : M ratios, which is consistent with the experimental observations.[23] Since both mechanisms start with the O–H bond breaking of methanol, followed by the dehydrogenation of methoxide to form formaldehyde, the main difference arises from the two elementary steps: $CH_2O^* + O^* \rightarrow H_2COO^* + ^*$ and $CH_2O^* + CH_3O^* \rightarrow CH_2OOCH_3^* + ^*$.

Fig. 1(c) shows the variation of reaction rates at different temperatures. It can be seen that at low temperatures, the elementary step of formaldehyde reacting with methoxy is dominant, while at higher temperatures, the oxidation of formaldehyde is dominant. The rates of these two elementary steps exhibit a crossing behavior at a specific temperature, and this temperature is lower when the S : M ratio is higher. This trend coincides with the observed change in the dominant mechanism. To further validate this trend, we also performed microkinetic simulations at an S : M ratio of 0.1, and the result (see Fig. S2 in the ESI†) is consistent with the observed trend, demonstrating the self-consistency of our findings.

3.3 Activity over Cu(111) and Cu(211)

Microkinetic simulations were further conducted to analyze the impact of reaction conditions on the overall reaction activity. Specifically, simulations were performed on the Cu (111) and Cu(211) surfaces at varied temperatures ranging from 498 K to 598 K and S : M ratios from 1 to 4. The reaction rate and the degree of rate control for methanol conversion were analyzed, as depicted in Fig. 2(a) and (b), respectively. The sum of the DRC coefficients under all conditions are provided in the ESI as Fig. S5.† The value of this sum fluctuates around 1 within the tolerance of numerical error. It was found that the elementary step of the dehydrogenation of methanol to form methoxy is the rate-controlling step under all reaction conditions, and therefore, its rate can be considered equal to the TOF for the methanol steam reforming process.

We derived a rate equation for the MSR reaction, as expressed in the following equation:

$$r = kp_{CH_3OH}\theta_*^2 = Ae^{-\frac{G_a}{k_BT}}p_{CH_3OH}\theta_*^2 \tag{8}$$

where r represents the TOF, k is the rate constant for the dehydrogenation of methanol to form methoxy, θ_* is the coverage of free active sites, A is the pre-exponential factor, G_a is the activation free energy, and p_{CH_3OH} is the partial pressure of methanol. Based on this equation, we were able to calculate the TOF under different conditions. The results were then compared with the TOF values calculated using the CatMAP software, as shown in the ESI as Fig. S3.† It was observed that the two sets of results matched well over both the Cu(111) and Cu(211) surfaces and under all the S : M ratios. This suggests that it is reasonable to represent the TOF with the reaction rate
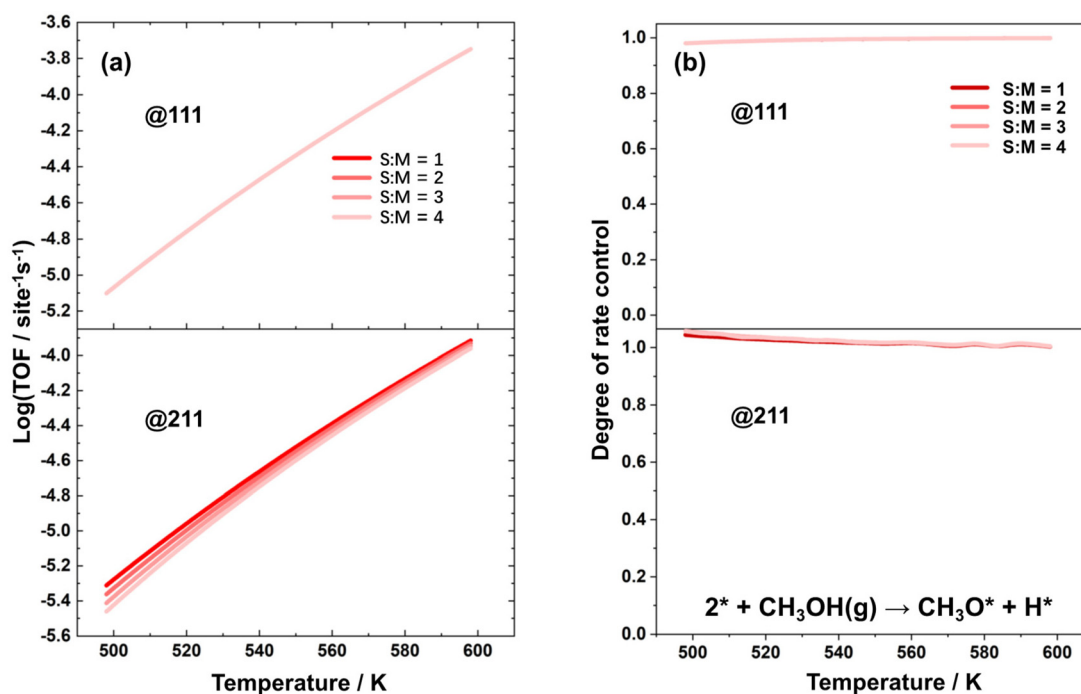

Fig. 2 (a) TOF of methanol over Cu(111) and Cu(211), as a function of temperature with different S : M ratios. (b) Degree of rate control for the elementary step of the dehydrogenation of methanol to form methoxy over Cu(111) and Cu(211) as a function of temperature with different S : M ratios.
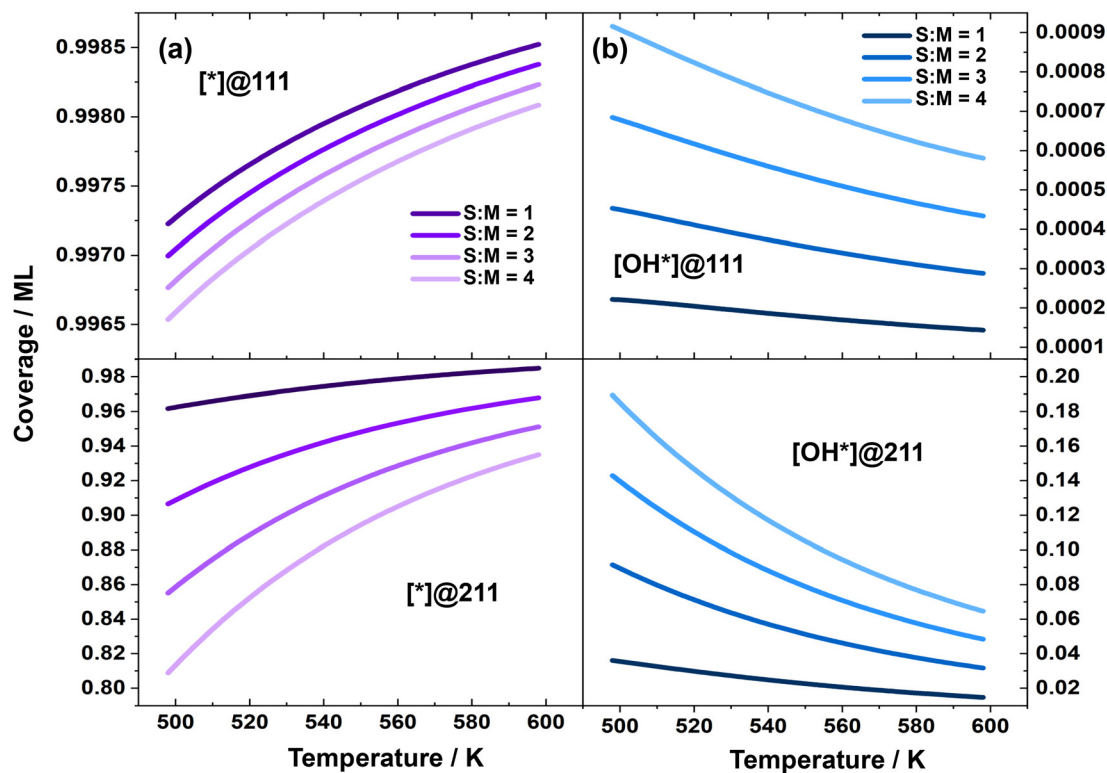
Fig. 3 (a) Coverage of free site; (b) logarithm of coverage of surface OH species over Cu(111) and Cu(211), in the MSR reaction, as a function of temperature with different S : M ratios.

of the dehydrogenation of methanol to form methoxy, which will greatly simplify the further analysis.

The derived rate equation demonstrates that the overall reaction activity is determined by several key factors, including the activation free energy of the dehydrogenation of methanol to form methoxy, the reaction temperature, the coverage of free active sites, and the partial pressure of methanol. Additionally, the free energy remains unchanged with variations in the S : M ratio. As a result, at a specific temperature and over a particular catalyst surface, the reaction activity becomes a function of the coverage of free active sites. Fig. 3 illustrates the logarithm of coverage of free active sites under different reaction conditions.

As shown in Fig. 2(a), the TOF over the Cu(111) surface remains relatively constant across different S : M ratios. However, over the Cu(211) surface, the TOF decreases significantly with higher S : M ratios. This observation aligns with the fact that the coverage of free active sites remains nearly constant under different S : M ratios over Cu(111), but decreases substantially with higher S : M ratios over Cu(211).

To further investigate the reason for the decrease in the coverage of free active sites with increasing S : M ratios, we examined the coverage of all surface species. Our analysis revealed that surface-adsorbed OH is the dominant species over these two surfaces. Therefore, we focused our study on the coverage of OH. Fig. 3 demonstrates that the change in OH coverage under different S : M ratios is minor over Cu(111), but signifi-
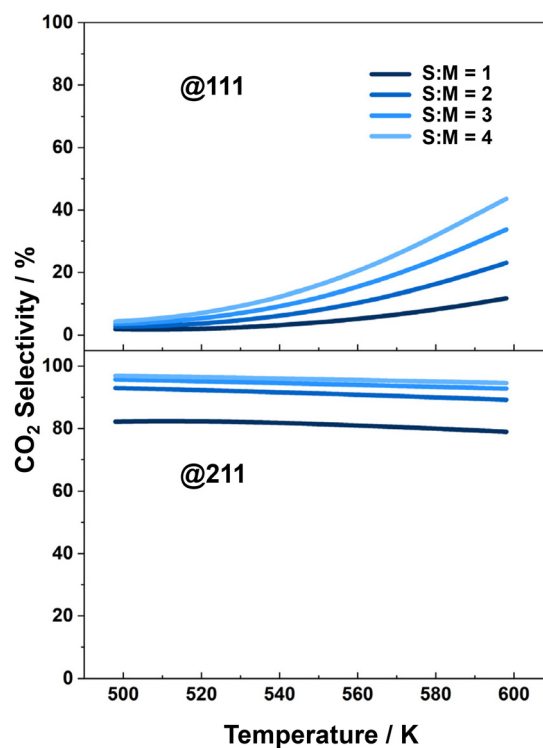

Fig. 4 CO_2 selectivity over Cu(111) and Cu(211), in MSR reaction, as a function of temperature, with different S : M ratios.

cant over Cu(211). According to the energies of the elementary steps, the reaction Gibbs free energy of $H_2O + * \rightarrow OH^* + \frac{1}{2}H_2$ is 0.24 eV higher over Cu(111) than over Cu(211), which may explain why OH* prefers to adsorb on the Cu(211) surface. The increasing coverage of OH* with higher S : M ratios is likely due to the higher water partial pressure, which leads to an elevated rate of H_2O dehydrogenation and subsequently results in a higher surface OH coverage. These are further supported by the detailed derivation for the coverage of free sites

and their relations with the reaction order and apparent activation energies as shown in the ESI.†

The activity over different catalyst surfaces is a function of both the free site coverage and the activation free energy at a particular temperature. Fig. S4 in the ESI† displays that the activation free energy of the dehydrogenation of methanol to form methoxy is slightly higher over the Cu(211) surface than over the Cu(111) surface. Additionally, Fig. 3 shows that the free site coverage is generally lower over the Cu(211)
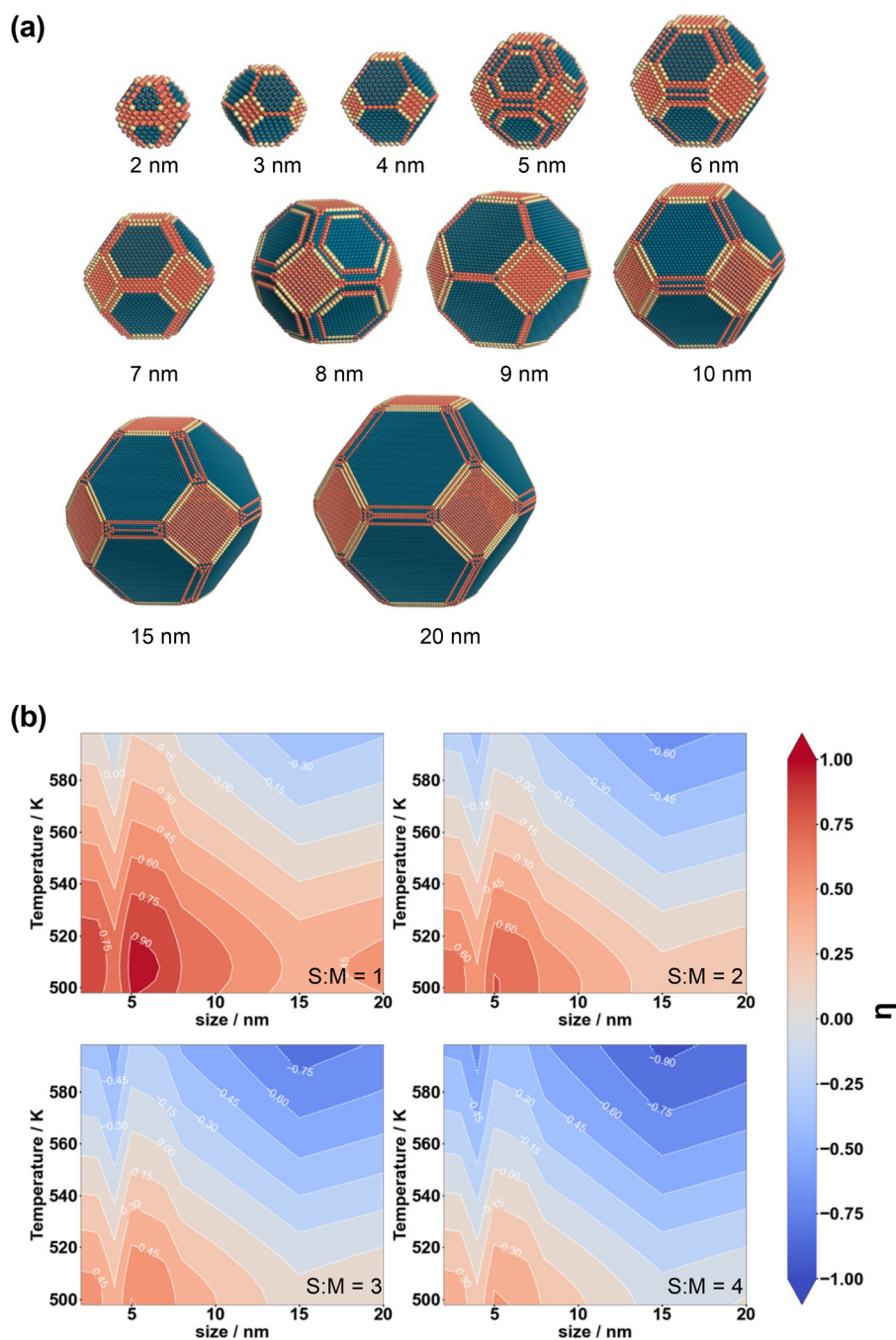

Fig. 5 (a) Structures of Cu nanoparticles with various sizes, where (211) and (111) surface sites highlighted in yellow and blue, respectively. (b) Logarithm of ratio of CO_2 yield over Cu(211) and Cu(111) under variant circumstances.

surface, which contributes to the fact that the activity over the Cu(111) surface is slightly higher than over the Cu(211) surface. Notably, the TOF over both surfaces at 498 K is on the order of magnitude of 10^{-5} per s per site, which is quite low. This result is consistent with the experimental observations that the maximum TOF based on surface sites of the MSR reaction over polycrystalline Cu foil is too low to be readily detected.[58]

3.4 Product selectivity and structure sensitivity

The CO_2 selectivity is another crucial property to consider for the MSR process, as CO is a poisonous byproduct that can deactivate the catalysts used in downstream hydrogen utilization. The selectivity of CO_2 under different reaction conditions over each catalyst surface is plotted in Fig. 4. The results indicate that the selectivity of CO_2 is higher over the Cu(211) surface than over the Cu(111) surface. In the research conducted by Li and co-workers,[59] CO_2 selectivity over Cu(111) ranges from approximately 10% to 40%, while over Cu(211) it varies from 60% to 90% at temperatures between 500 K and 600 K, the temperature range considered in our work. Meanwhile, our study reports a CO_2 selectivity ranges from 0 to 40% over Cu(111) and from 75% to 80% over Cu(211), which aligns closely with the findings presented by Li and co-workers. Over both surfaces, the selectivity increases with increasing S : M ratio. Furthermore, we found that although the activity of the MSR reaction over the Cu(111) surface is slightly higher than over the Cu(211) surface, the low CO_2 selectivity over the Cu(111) surface makes it less advantageous for further application in hydrogen production. Thus, it would be insightful to study the structure sensitivity of the catalytic performance to determine the optimal facet for practical applications. It should be noted that we selected these two surfaces because they represent typical surface step and flat sites that are extensively studied in the majority of theoretical and surface science works. Consequently, our comparison focuses solely on the preference between these two sites.

To study the structure sensitivity of the MSR reaction, we constructed Cu nanoparticle models with different sizes according to the Wulff construction method, and the corresponding structures are presented in Fig. 5(a). We then accurately determined the number of both Cu(111) and Cu(211) surface sites. In order to assess the catalyst performance more comprehensively, we employed the formation rate of CO_2 as a metric of activity, as it can effectively capture both the activity of reactant consumption and the selectivity of CO_2 production. The logarithm of the ratio of the CO_2 formation rates over different S : M ratios, temperatures, and nanoparticle sizes, denoted as η, was calculated using the following formula:

$$\eta = \log\left(\frac{r(CO_2)_{211} \cdot n_{211}}{r(CO_2)_{111} \cdot n_{111}}\right) \quad (9)$$

where $r(CO_2)_{211}$ and $r(CO_2)_{111}$ represent the formation rates of CO_2 over the Cu(211) and Cu(111) facets, respectively, and n_{211} and n_{111} denote the number of Cu(211) and Cu(111) surface sites, respectively.

The results are presented in Fig. 5(b). According to Fig. 5(b), a positive value of the logarithm of the ratio indicates a greater contribution from the Cu(211) facet. In most scenarios, the Cu(211) facet exhibits a more substantial contribution than the Cu(111) facet. The figure reveals that at lower S : M ratios, lower temperatures, and smaller particle sizes, the CO_2 yield over the Cu(211) facet is notably higher compared to that over the Cu(111) facets.

4. Conclusions

In this study, we investigated the trends of reaction activity, product selectivity, and mechanism selectivity under various reaction conditions over both the Cu(111) and Cu(211) surfaces. Throughout the study, the reaction mechanism over the Cu(211) surface was found to be the H_2COO mechanism. In contrast, over the Cu(111) surface, both the methyl formate and H_2COO mechanisms were observed, with the former occurring only at low temperatures and low S : M ratios. These findings are consistent with the available experimental observations. The reaction activity over the Cu(111) surface was slightly higher than over the Cu(211) surface. Since the rate-controlling transition state for the entire reaction could be identified through the DRC analysis, we were able to derive a rate equation that can quantitatively explain the trend of activity under different reaction conditions. Furthermore, we found that the CO_2 selectivity was significantly higher over the Cu(211) surface than over the Cu(111) surface. The copper nanoparticle models of different sizes built based on the Wulff construction scheme make the calculations of the amounts of the (211) and (111) surface sites for each nanoparticle possible. After carrying out a detailed structure sensitivity study, we found that at lower S : M ratios, lower temperatures, and smaller particle sizes, the CO_2 yield over the (211) facet is higher compared to that over the (111) facet. This finding will be instructive for the future design of improved catalysts.

Data availability

The data supporting this article have been included as part of the ESI.†

Conflicts of interest

There are no conflicts to declare.

Acknowledgements

ShanghaiTech University and Shanghai Supercomputer Center for computing time.

References

1 G. E. Halkos and E.-C. Gkampoura, *Renewable Sustainable Energy Rev.*, 2021, **144**, 110981.

2 L. Li, W. Zeng, M. Song, X. Wu, G. Li and C. Hu, *Catalysts*, 2022, **12**, 244.

3 Y. Pan and F. Dong, *Technol. Forecast. Soc. Change*, 2022, **176**, 121475.

4 H. Wang, in *Waste to Renewable Biohydrogen*, Elsevier, 2023, pp. 195–210.

5 X. Wang, S. Bi, J. Zhang and H. Tao, *Catalysts*, 2022, **12**, 204.

6 M. Oikawa, Y. Kojiya, R. Sato, K. Goma, Y. Takagi and Y. Mihara, *Int. J. Hydrogen Energy*, 2022, **47**, 1319–1327.

7 M. Yue, H. Lambert, E. Pahon, R. Roche, S. Jemei and D. Hissel, *Renewable Sustainable Energy Rev.*, 2021, **146**, 111180.

8 I. Dincer, *Int. J. Hydrogen Energy*, 2012, **37**, 1954–1971.

9 J. Zhao, R. Shi, Z. Li, C. Zhou and T. Zhang, *Nano Sel.*, 2020, **1**, 12–29.

10 D. Güllü and A. Demirbaş, *Energy Convers. Manage.*, 2001, **42**, 1349–1356.

11 T. Chmielniak and M. Sciazko, *Appl. Energy*, 2003, **74**, 393–403.

12 D. R. Palo, R. A. Dagle and J. D. Holladay, *Chem. Rev.*, 2007, **107**, 3992–4021.

13 A. D. Le and B. Zhou, *J. Power Sources*, 2008, **182**, 197–222.

14 S. Sá, H. Silva, L. Brandão, J. M. Sousa and A. Mendes, *Appl. Catal., B*, 2010, **99**, 43–57.

15 J. Amphlett, M. Evans, R. Mann and R. Weir, *Can. J. Chem. Eng.*, 1985, **63**, 605–611.

16 H. Kobayashi, N. Takezawa and C. Minochi, *Chem. Lett.*, 1976, **5**, 1347–1350.

17 E. Santacesaria and S. Carra, *Appl. Catal.*, 1983, **5**, 345–358.

18 D. R. Palo, R. A. Dagle and J. D. Holladay, *Chem. Rev.*, 2007, **107**, 3992–4021.

19 N. Takezawa and N. Iwasa, *Catal. Today*, 1997, **36**, 45–56.

20 K. Takahashi, N. Takezawa and H. Kobayashi, *Appl. Catal.*, 1982, **2**, 363–366.

21 C. Jiang, D. Trimm, M. Wainwright and N. Cant, *Appl. Catal., A*, 1993, **97**, 145–158.

22 B. A. Peppley, J. C. Amphlett, L. M. Kearns and R. F. Mann, *Appl. Catal., A*, 1999, **179**, 31–49.

23 Y. Choi and H. G. Stenger, *Appl. Catal., B*, 2002, **38**, 259–269.

24 S. Lin, D. Xie and H. Guo, *ACS Catal.*, 2011, **1**, 1263–1271.

25 G. Kresse and J. Furthmüller, *Phys. Rev. B: Condens. Matter*, 1996, **54**, 11169.

26 G. Kresse and J. Hafner, *Phys. Rev. B: Condens. Matter*, 1993, **47**, 558.

27 G. Kresse and D. Joubert, *Phys. Rev. B: Condens. Matter*, 1999, **59**, 1758.

28 J. Wellendorff, K. T. Lundgaard, A. Møgelhøj, V. Petzold, D. D. Landis, J. K. Nørskov, T. Bligaard and K. W. Jacobsen, *Phys. Rev. B: Condens. Matter*, 2012, **85**, 235149.

29 H. Wu and B. Yang, *Appl. Surf. Sci.*, 2023, **614**, 156116.

30 P. Wu and B. Yang, *Catal. Sci. Technol.*, 2019, **9**, 6102–6113.

31 D. Xu, P. Wu and B. Yang, *J. Phys. Chem. C*, 2019, **123**, 8959–8966.

32 K. Yang and B. Yang, *J. Phys. Chem. C*, 2018, **122**, 10883–10891.

33 W. Zhu and B. Yang, *J. Phys. Chem. C*, 2021, **125**, 18743–18751.

34 F. Studt, F. Abild-Pedersen, J. B. Varley and J. K. Nørskov, *Catal. Lett.*, 2013, **143**, 71–73.

35 S. Gautier, S. N. Steinmann, C. Michel, P. Fleurat-Lessard and P. Sautet, *Phys. Chem. Chem. Phys.*, 2015, **17**, 28921–28930.

36 A. J. Medford, J. Sehested, J. Rossmeisl, I. Chorkendorff, F. Studt, J. K. Nørskov and P. G. Moses, *J. Catal.*, 2014, **309**, 397–407.

37 H. Thirumalai and J. R. Kitchin, *Surf. Sci.*, 2016, **650**, 196–202.

38 M. Methfessel and A. Paxton, *Phys. Rev. B: Condens. Matter*, 1989, **40**, 3616.

39 A. Alavi, P. Hu, T. Deutsch, P. L. Silvestrelli and J. Hutter, *Phys. Rev. Lett.*, 1998, **80**, 3650.

40 A. Michaelides, Z.-P. Liu, C. Zhang, A. Alavi, D. A. King and P. Hu, *J. Am. Chem. Soc.*, 2003, **125**, 3704–3705.

41 M. Cieplak, M. Henkel, J. Karbowski and J. R. Banavar, *Phys. Rev. Lett.*, 1998, **80**, 3654.

42 L. Liu, B. McAllister, H. Ye and P. Hu, *J. Am. Chem. Soc.*, 2006, **128**, 4017–4022.

43 B. Yang, X.-Q. Gong, H.-F. Wang, X.-M. Cao, J. J. Rooney and P. Hu, *J. Am. Chem. Soc.*, 2013, **135**, 15244–15250.

44 X.-P. Wu and X.-Q. Gong, *J. Am. Chem. Soc.*, 2015, **137**, 13228–13231.

45 J. Wellendorff, T. L. Silbaugh, D. Garcia-Pintos, J. K. Nørskov, T. Bligaard, F. Studt and C. T. Campbell, *Surf. Sci.*, 2015, **640**, 36–44.

46 X. Fu, W. Shen, T. Yao and W. Hou, *Physical Chemistry*, Higher Education Press, 2005.

47 A. J. Medford, C. Shi, M. J. Hoffmann, A. C. Lausche, S. R. Fitzgibbon, T. Bligaard and J. K. Nørskov, *Catal. Lett.*, 2015, **145**, 794–807.

48 C. H. Shomate, *J. Phys. Chem.*, 1954, **58**, 368–372.

49 C. A. Wolcott, A. J. Medford, F. Studt and C. T. Campbell, *J. Catal.*, 2015, **330**, 197–207.

50 C. T. Campbell, *ACS Catal.*, 2017, **7**, 2770–2779.

51 Y.-X. Wang, H.-L. Zhang, P. An, H.-S. Wu and J.-F. Jia, *J. Phys. Chem. C*, 2021, **125**, 20905–20918.

52 X.-K. Gu and W.-X. Li, *J. Phys. Chem. C*, 2010, **114**, 21539–21547.

53 S. Lin, D. Xie and H. Guo, *J. Phys. Chem. C*, 2011, **115**, 20583–20589.

54 Z.-J. Zuo, L. Wang, P.-D. Han and W. Huang, *Int. J. Hydrogen Energy*, 2014, **39**, 1664–1679.

55 S. Lin, R. S. Johnson, G. K. Smith, D. Xie and H. Guo, *Phys. Chem. Chem. Phys.*, 2011, **13**, 9622–9631.

56 T. Gu, B. Wang, S. Chen and B. Yang, *ACS Catal.*, 2020, **10**, 6346–6355.

57 B. Wang, S. Chen, J. Zhang, S. Li and B. Yang, *J. Phys. Chem. C*, 2019, **123**, 30389–30397.

58 L. Mayr, X. Shi, N. Köpfle, B. Klötzer, D. Y. Zemlyanov and S. Penner, *J. Catal.*, 2016, **339**, 111–122.

59 S.-S. Wang, X.-K. Gu, H.-Y. Su and W.-X. Li, *J. Phys. Chem. C*, 2018, **122**, 10811–10819.